

Altitude-Aware Visual Place Recognition in Top-Down View

Xingyu Shao¹, Mengfan He¹, Chunyu Li¹, Liangzheng Sun¹ and Ziyang Meng¹, *Senior Member, IEEE*

Abstract—To address the challenge of aerial visual place recognition (VPR) problem under significant altitude variations, this study proposes an altitude-adaptive VPR approach that integrates ground feature density analysis with image classification techniques. The proposed method estimates airborne platforms’ relative altitude by analyzing the density of ground features in images, then applies relative altitude-based cropping to generate canonical query images, which are subsequently used in a classification-based VPR strategy for localization. Extensive experiments across diverse terrains and altitude conditions demonstrate that the proposed approach achieves high accuracy and robustness in both altitude estimation and VPR under significant altitude changes. Compared to conventional methods relying on barometric altimeters or Time-of-Flight (ToF) sensors, this solution requires no additional hardware and offers a plug-and-play solution for downstream applications, making it suitable for small- and medium-sized airborne platforms operating in diverse environments, including rural and urban areas. Under significant altitude variations, incorporating our relative altitude estimation module into the VPR retrieval pipeline boosts average R@1 and R@5 by 29.85% and 60.20%, respectively, compared with applying VPR retrieval alone. Furthermore, compared to traditional Monocular Metric Depth Estimation (MMDE) methods, the proposed method reduces the mean error by 202.1 m, yielding average additional improvements of 31.4% in R@1 and 44% in R@5. These results demonstrate that our method establishes a robust, vision-only framework for three-dimensional visual place recognition, offering a practical and scalable solution for accurate airborne platforms localization under large altitude variations and limited sensor availability.

Index Terms—Visual Place Recognition (VPR), Airborne Platforms, Relative Altitude Estimation, Coarse Localization, Plug-and-Play Solution, Unmanned Aerial Vehicle (UAV)

I. INTRODUCTION

AERIAL Visual Place Recognition (VPR) plays a crucial role in enabling robust localization for airborne platforms across diverse operational scenarios. However, many existing aerial VPR approaches rely on the strong assumption that the flight altitude is known and remains constant throughout the whole flight. On the other hand, one of the primary challenges in aerial Visual Place Recognition (VPR), compared to ground-based handheld or vehicle-mounted systems, is the large freedom in altitude variation. It is clear that aligning the capture

altitude of query and database images during unmanned aerial vehicle (UAV) initialization and localization is critical. For VPR, this scale quantity is the platform’s relative altitude — its vertical distance above ground level (AGL) — which directly determines image scale and appearance.

Barometric altimeters measure absolute (barometric) altitude with respect to an altimeter setting (e.g., QNH: altimeter setting to indicate elevation above mean sea level, or QFE: altimeter setting to indicate height above a specific airfield elevation), which is fundamentally different from AGL. Conventional platforms derive mean-sea-level altitude from barometric sensors and onboard/linked elevation data, then subtract local ground elevation to obtain AGL relative altitude. Without high-fidelity terrain or ground reference, this conversion is unreliable, even with perfect atmospheric modeling. Platforms lacking accurate geospatial or terrain information often rely on time-of-flight (ToF) sensors for relative altitude measurement. ToF sensors are broadly categorized as indirect ToF (iToF) and direct ToF (dToF). iToF is sensitive to ambient illumination, exhibits higher noise, and operates over a limited altitude range. In contrast, dToF offers stronger interference resilience and a more flexible operating range. However, dToF modules are generally tailored for larger platforms. Their size-weight-power (SWaP) demands often exceed small-to-medium UAV payload budgets. Given the ubiquity of cameras on small UAVs and the constraints of conventional sensors, there is a clear need for robust, vision-only altitude estimation solution.

Motivated by these observations, this paper proposes to transform spatial-domain images into the frequency domain via a two-dimensional Fast Fourier Transform (FFT), and apply a nonlinear mapping to infer relative altitude from the density and distribution of ground features. The resulting representation is highly sensitive to scale variations induced by altitude changes. We then discretize the estimated altitude into classes and perform altitude-aware cropping of the original images to produce normalized primitive views. These uniformly scaled images can then serve as input for any VPR pipeline, thereby establishing an integrated workflow encompassing altitude estimation, image preprocessing, and robust image retrieval. This altitude prior regularizes scale in feature extraction and improves cross-altitude matchability. The proposed system enables three-dimensional aerial initialization using solely visual input, and can further enable subsequent fine-grained matching. The proposed plug-and-play framework requires no additional hardware and avoids the limitations of dense monocular metric depth estimation in aerial scenarios. Extensive experiments across diverse terrains demonstrate that our method achieves high accuracy and robustness, outper-

This work was supported in part by a grant of the National Nature Science Foundation of China under Grant 62403269. (Mengfan He and Chunyu Li contributed equally to this work.) (Corresponding author: Ziyang Meng.)

Xingyu Shao, Mengfan He, Chunyu Li and Ziyang Meng are with the Department of Precision Instrument, Tsinghua University, Beijing 100084, China (e-mail: shao-xy21@mails.tsinghua.edu.cn; hmf21@mails.tsinghua.edu.cn; lcyfly1@163.com; ziyangmeng@tsinghua.edu.cn).

Liangzheng Sun is with the School of Instrumentation Science and Optoelectronics Engineering, Beijing Information Science and Technology University, Beijing 100192, China (e-mail: 2023030031@bistu.edu.cn).

forming traditional approaches. In this study, we propose an altitude-adaptive VPR framework that integrates ground feature density analysis with advanced image classification techniques. Our key contributions are summarized as follows:

- We propose a vision-only approach that estimates relative altitude (AGL) by analyzing frequency-domain features extracted via 2D FFT. This method captures altitude-sensitive variations in ground-feature density and reformulates altitude estimation as a classification task by discretizing flight ranges and learning class prototypes.
- We propose a novel Quality Adaptive Margin Classifier (QAMC), which adaptively adjusts the classification margin based on feature quality. This classifier employs a feature-norm-aware margin loss to learn more discriminative embeddings and improve robustness under diverse conditions, significantly enhancing VPR performance.
- We incorporate an altitude-aware cropping mechanism that normalizes input images into resolution-consistent primitive views, aligning the observation altitudes of queries with the reference map and improving cross-altitude compatibility.

The remainder of this paper is organized as follows. Section II reviews representative VPR methods and explains why monocular metric depth estimation (MMDE) is unsuitable for our task. Section III presents the proposed approach under varying flight altitudes. Section IV describes the collected dataset, outlines the experimental setup, and reports evaluation results under diverse conditions. Section V summarizes the conclusions and key findings.

II. RELATED WORKS

In this work, we address visual place recognition (VPR) problem on airborne platforms with altitude variations. Conventional aerial VPR methods assume a constant flight altitude, while real applications involve unknown, dynamically varying altitudes that make scale-invariant assumption invalid. We first review the related works. In particular, Section II-A focuses on the development of VPR, Section II-B examines the adaptation of VPR to airborne platforms, and Section II-C reviews Monocular Metric Depth Estimation (MMDE) methods, which are designed for dense, limited-range depth inference, and analyzes why those methods are unsuitable for coarse altitude estimation problem for airborne platforms.

A. Visual Place Recognition (VPR)

In training methods for Visual Place Recognition (VPR) models, two primary pipelines have emerged: retrieval-based approaches and classification-based approaches. The vast majority of VPR studies adopt the retrieval-based pipeline, whose fundamental idea is to obtain the predicted coordinates by performing a similarity search over a pre-constructed embedding database. These embeddings may be generated via two techniques: one involves extracting local feature descriptors followed by non-differentiable manual clustering algorithms [1]–[4]; the other produces global feature representations through end-to-end differentiable deep aggregators [4]–[10]. Currently, the management and retrieval of these high-dimensional deep

features are commonly facilitated by open-source libraries such as FAISS [11], [12].

In recent years, deep feature extractors based on Convolutional Neural Networks (CNNs) or Transformers have become mainstream solution. Among CNN-based models, the ResNet series [13], ResNeXt [14], the EfficientNet series [15], [16], and ConvNeXt [17], [18] have demonstrated remarkable performance. Based on Transformer architectures, the foundation model DINOv2 [19] has gained significant attention due to its robust feature extraction capabilities, inspiring subsequent works such as CricaVPR [20] and DINOv2-SALAD [21]. For deep feature aggregation, NetVLAD is widely employed as a representative aggregation layer. Additionally, recent aggregators like MixVPR have shown excellent performance in processing CNN-generated deep features. Common pooling operations include GeM (Generalized-Mean pooling) [22], spatial max-pooling [23], and R-MAC (Regional Maximum Activation of Convolutions) [24]. Readers are referred to [25]–[27] for further details on retrieval-based VPR approaches. During training, these methods typically employ triplet loss [28] or quadruplet loss [29] to optimize distances in the feature space [5]. However, this process generally requires exhaustive mining of positive and negative samples within each training batch. Such mining not only increases computational and resource demands but also, in the context of large-scale datasets, the time and storage required for mining appropriate negative samples tend to grow exponentially (often with a complexity of $O(n)$). Moreover, traditional mining methods, such as those based on triplet loss, often exhibit slow convergence on large datasets. One potential solution to this issue is to leverage the intrinsic characteristics of the data through lightweight data mining. Although lightweight mining strategies such as Graded Similarity Mining [30] can partially mitigate the computational burden, they either fail to fully exploit the entire dataset or require complex data preparation, therefore limiting model generalization and efficiency across different scenarios.

Beyond retrieval-based approaches, visual place recognition (VPR) has also been framed as a classification problem, where images are assigned to predefined geographic cells. Early works focused on global scales. For example, PlaNet [31] use Google’s S2 geometry library to partition the Earth into adaptive cells and trained a deep network to predict image region. Vo et al. [32] combined such classification features with retrieval via kernel density estimation. Kordopatis-Zilos et al. [33] fused EfficientNet-based classification with retrieval. Theiner et al. [34] semantically partition the globe into meaningful regions to enhance interpretability in geolocation. Izbicki et al. [35] use a mixture of von Mises-Fisher distributions to model geospatial cell distributions on the Earth’s sphere. Classification methods benefit from low complexity and fast inference, but accuracy hinges on partition granularity: more cells improve precision but inflate parameters and reduce per-class training data. To address this trade-off, several hierarchical and composite schemes excel at urban-scale localization problem. Muller-Budack et al. proposed Hierarchical Geolocation Estimation (HGE) [36], which applies coarse-to-fine Earth partitions so that multi-scale

context refines predictions. HGE outperforms PlaNet in city-scale tasks even with less data. CPlaNet [37] cross-combines multiple coarse partitions into fine cells, achieving significant gains in street-level retrieval accuracy by leveraging several classifiers jointly. Focusing specifically on urban and fine-grained VPR, Gronat et al. [38] first showed that an SVM classifier can localize within a 1.56 km² area. More recently, CosPlace [39] discretized UTM coordinates and image orientation into city-scale classes, grouping nonadjacent cells to balance data and training independent models per group, and employed CosFace loss [40] during training while still using retrieval at inference. Divide & Classify (D&C) [41] is further simplified into uniform square UTM grids, adopting ArcFace (Additive Angular Margin) loss to build an Additive Angular Margin Classifier (AAMC) and predicting a query’s location by matching its feature to prototype vectors. Recent cross-view geo-localization studies also highlight the importance of local and multi-scale modeling. Patch Similarity Self-Knowledge Distillation (PSSKD) [42] enforces patch-level correspondence via self-distillation to improve cross-view retrieval, while multi-scale attention encoders [43] capture hierarchical context and mitigate domain discrepancies between street-level and aerial imagery. These works complement retrieval and classification pipelines by enhancing robustness under drastic viewpoint changes, yet they typically assume fixed-scale conditions rather than dynamically varying altitudes.

In summary, recent advances in VPR reveal a shift from retrieval-based pipelines toward classification-based strategies that exploit spatial partitioning and adaptive learning to enable scalable and fine-grained localization in aerial and urban scenes.

B. VPR for Airborne Platforms

Visual localization techniques have achieved widespread applications in various systems, particularly on ground vehicles and handheld devices [25], [44]–[46]. Nonetheless, localization solutions specifically devised for airborne platforms remain relatively underexplored. This disparity stems from fundamental differences in data acquisition modalities, spatial resolution, and viewing geometries. Unlike ground platforms, airborne platforms — encompassing both unmanned and manned vehicles operating at varying altitudes — exhibit more complex motion patterns and higher degrees of freedom, which in turn results in substantial variations in captured viewpoints and scene content. To address these challenges, a variety of methods have been proposed. Early work such as Deep Urban Signature (DUS) [47] demonstrates the feasibility of CNN-based localization in GPS-denied urban environments by extracting semantic features using a pre-trained VGG16 [48] network. Building on this work, Patel et al. [49] introduced a global pose estimation framework that integrates pre-rendered Google Earth imagery and dense image registration techniques. For lightweight onboard deployment, Samano et al. [50] employed compact image descriptors derived from the Mastermap database to balance computational efficiency and system robustness. Descriptor-level improvements have also been explored: Mantelli et al. [51] developed a noise-

resistant abBRIEF operator, while Bianchi et al. [52] proposed an autoencoder-based compression strategy to accelerate real-time localization from satellite imagery. More recently, AirGeoNet [53] enables direct retrieval over geo-referenced remote-sensing maps using pretrained DINOv2 [19] features. The EAGLe Framework [54] and F3-Net [55] further achieve high-performance cross-view image retrieval tailored for UAV-based scenarios. Additionally, recent studies [56], [57] introduced probabilistic fusion and multi-map reasoning techniques to improve localization performance and stability in large-scale, dynamic environments. GeoCluster [58] enhances UAV-based VPR by aggregating descriptors through spatial clustering, improving robustness against viewpoint and appearance variations without altering backbone complexity. Beyond single-modality approaches, multi-modal aerial-ground frameworks have also been explored: a Neural ODE-based model [59] aligns heterogeneous modalities such as camera and LiDAR across aerial-ground views, demonstrating the promise of continuous-time modeling for cross-domain place recognition. GeoVINS [60] extended classify-then-retrieve VPR to UAV platforms, demonstrating that airborne geolocalization can benefit from city-scale classification before feature matching.

Together, these studies reflect a growing shift toward aerial-specific localization techniques that combine semantic understanding, cross-view retrieval, spatial-domain clustering, and multi-modal fusion to overcome the unique challenges posed by altitude variation, viewpoint diversity, and sensor limitations on airborne platforms.

C. Monocular Metric Depth Estimation (MMDE)

Our task specifically targets the scenario of estimating a global relative altitude (AGL) from a single nadir-view image to support altitude-aware VPR. Since this is a novel problem, no vision-only baseline currently exists. In current UAV systems, altitude information can be obtained via digital elevation model (DEM) alignment or barometric/altimeter sensors, but these approaches rely on external data and hardware and therefore cannot serve as comparable baselines for evaluating vision-only methods. For this reason, we clarify that monocular metric depth estimation (MMDE) methods are included only as contextual references rather than direct baselines. We chose MMDE because among vision-based approaches they are the closest to our task, as they infer geometric quantities from a single image.

MMDE seeks to determine the camera-to-object distance from a single image. Recent general-purpose approaches — such as Depth Anything V2 [61], UniDepth V2 [62], and Metric3Dv2 [63] can be deployed zero-shot in a wide variety of scenarios without further fine-tuning. Depth Anything V2 [61] uses large teacher models and pseudo-labeled synthetic data, complemented by unannotated real-world images, to enhance model generalization. UniDepth V2 employs camera prompts and diverse input scales to promote geometric invariance and robustness across varying scenarios, while Metric3Dv2 normalizes training data into a unified camera space to alleviate depth blurriness. Additional works, including ZoeDepth [64],

PatchFusion [65], and Depth Pro [66], further improve the performance of MMDE. Despite these advancements, research on MMDE for aerial imagery remains limited. TanDepth [67] leverages UAV imagery primarily for the construction of digital elevation models. Miclea et al. [68] propose a semantically-guided dynamic monocular depth estimator for low-altitude UAVs.

In practice, directly applying MMDE networks to airborne relative altitude estimation is not feasible. Unlike conventional MMDE, which aims to generate dense pixel-wise depth maps, aerial altitude estimation requires only a coarse, global measure to support tasks such as VPR. As flight altitude increases, ground features become smaller and less distinct, reducing the effectiveness of localized contextual cues that dense depth models rely on. These limitations can be summarized as follows:

- 1) **Lack of Annotated Data:** Dense depth estimation models typically rely on pixel-wise annotations for supervised training or fine-tuning, yet such fine-grained datasets are scarce for high-altitude airborne platforms, thereby impeding effective model adaptation.
- 2) **Limited Operational Range:** Conventional depth estimation methods are generally optimized for ranges on the order of one hundred meters, whereas many airborne platforms operate far beyond this threshold.
- 3) **Lack of Local Features:** Remote sensing images, typically captured from high altitudes, provide low spatial resolution and exhibit a more limited range of fine-grained local features than low-altitude aerial images. Their near-nadir view and the inherent loss of details reduce the richness of contextual cues, which are critical for monocular depth estimation methods.

III. METHODOLOGY

We formulate our task as an aerial VPR problem under unknown and variable flight altitudes. Given a query image I_{in} captured by an airborne platform at an unknown altitude, the goal is to estimate its relative altitude and retrieve the corresponding map tiles from a geo-referenced database constructed at the same altitude.

As illustrated in Fig. 1, the proposed framework consists of two core modules — a relative altitude estimation module and a VPR module — that jointly process I_{in} in a two-stage pipeline. The altitude estimation module estimates the airborne platform’s relative altitude H as H_{estimate} , guiding an altitude-adaptive cropping and scaling of I_{in} to match the spatial scale of reference map tiles. The VPR module then retrieves candidate reference images via a feature-based search of any VPR pipeline, referred to as AVPR. Formally, the considered problem is solved using the following operators:

$$H_{\text{estimate}} = (\text{Class2Alt} \circ \text{AC} \circ \text{Spat2Freq})(I_{\text{in}}), \quad (1)$$

and

$$(\mathcal{V}, \mathcal{U}) = (\text{AVPR} \circ \text{Crop})(I_{\text{in}}), \quad (2)$$

where $\mathcal{V} = \{d_i \in \mathbb{R}^C\}_{i=1}^{n_{\text{retrieve}}}$ denotes the set of retrieved global feature vectors, and $\mathcal{U} = \{\text{UTM}_i\}_{i=1}^{n_{\text{retrieve}}}$ represents their

corresponding geo-coordinates. In compact form, the overall pipeline is expressed as:

$$(H_{\text{estimate}}, \mathcal{V}, \mathcal{U}) = \text{AE-VPR}(I_{\text{in}}). \quad (3)$$

Each operator defined in Equations (1)-(2) will be elaborated in the following sections. Before detailing each operator, we first illustrate representative query samples to provide intuition. To provide a clearer illustration of the query image preparation across different datasets, we show representative examples in Fig. 2. This schematic diagram visualizes the processing pipeline, including raw input, frequency-domain representation, and cropped primitive images, which complement the overall workflow shown in Fig. 1. For the relative altitude estimation module, we first introduce the image pre-processing technique *Spat2Freq* in Section III-A1, followed by the altitude classification operation *AC* in Section III-A2, and the class-to-altitude mapping function *Class2Alt* in Section III-A3. For the VPR module, Section III-B1 presents the primitive image extraction method *Crop*, Section III-B2 details the classification-based retrieval process *AVPR*, and Section III-C describes the *Quality Adaptive Margin Classifier (QAMC)* used in the classification process above. Although the adopted operations such as 2D FFT and altitude-aware cropping are individually simple, their novelty lies in the task-driven combinations. We reformulate relative altitude estimation as a classification problem, and the estimated altitude guides cropping to normalize query images for cross-altitude retrieval. Together with the proposed *Quality Adaptive Margin Classifier (QAMC)*, this pipeline provides a unified solution for altitude-aware VPR problem and achieves impressive results.

A. Relative Altitude Estimation Module

The relative altitude estimation module takes the aerial images captured downward by the camera as input and infers the approximate average altitude of the airborne platform relative to the ground from the aerial image. The purpose of this module is to obtain a magnification factor for the original image, so as to acquire the primitive image at the estimated altitude.

Since VPR exhibits a certain degree of robustness to altitude variations, and we therefore regard the relative altitude estimation problem as a classification task.

1) *Image Pre-processing:* In regions where ground features are sparse, aerial images captured by airborne platforms in a top-down view exhibit limited sensitivity to scale variations induced by altitude changes in the spatial domain. On the other hand, the frequency domain demonstrates significantly high sensitivity to such variations. We choose to apply a two-dimensional Fast Fourier Transform (FFT) to the three channels (RGB) of the visible image and perform a nonlinear mapping on the amplitude spectrum before feeding it into the CNN backbone.

Specifically, let the three channels of the original RGB image be denoted by $I_c(x, y)$, $c \in \{R, G, B\}$. First, a two-

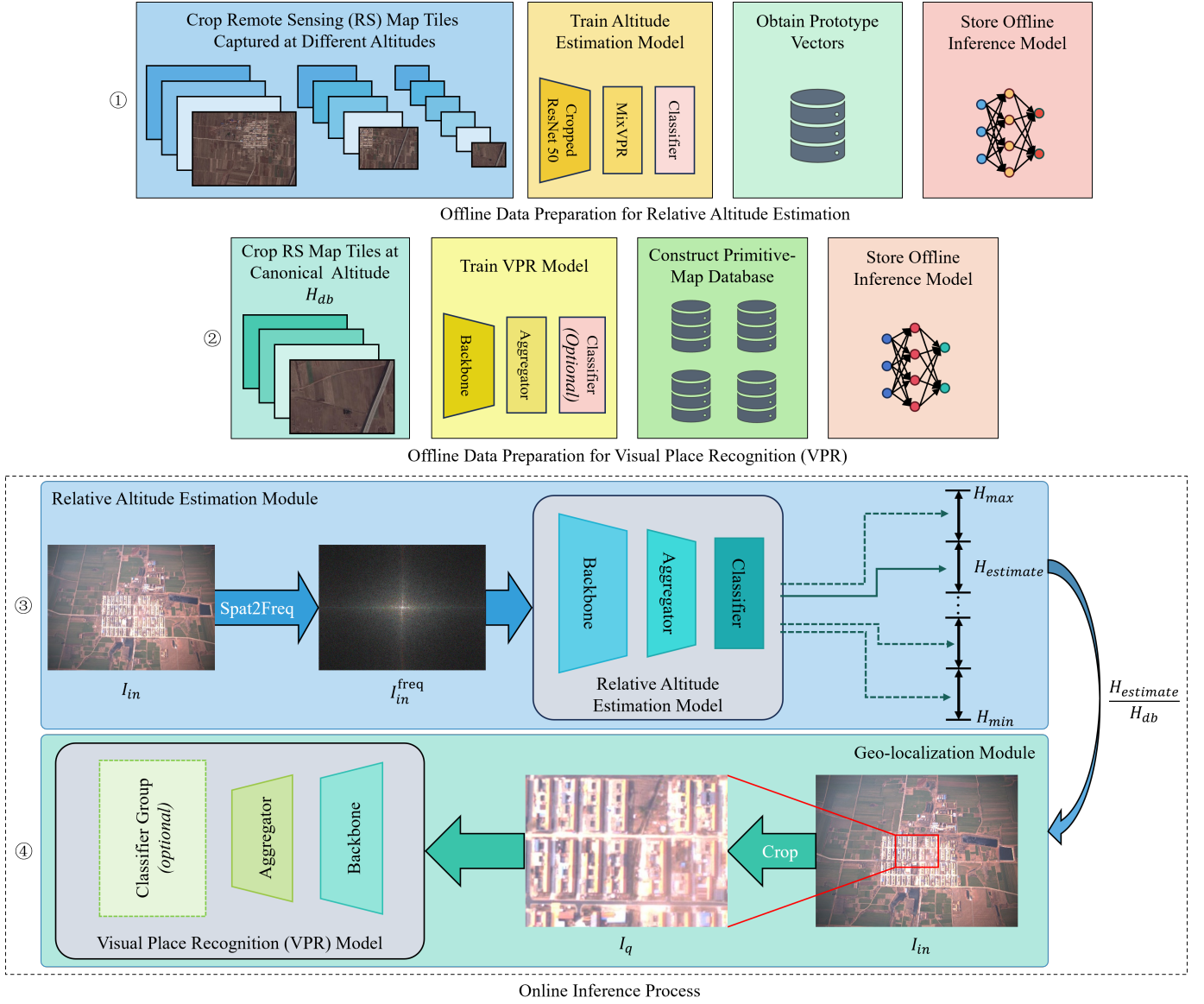


Fig. 1. Overall pipeline for relative altitude estimation and visual place recognition (VPR). The pipeline proceeds sequentially from steps ① to ④, where steps ① and ② are offline preparation stages and steps ③ and ④ are online inference stages.

dimensional FFT is applied on each channel:

$$I_{in} = [I_R, I_G, I_B] \quad (4)$$

$$F_c(u, v) = \mathcal{F}(I_c(x, y)), \quad c \in \{R, G, B\}, \quad (5)$$

where \mathcal{F} represents the FFT operation and I_c denotes the c -th channel of input image I_{in} . Next, we shift the zero-frequency component to the center of the image, and then centralizes the Fourier spectrum such that the frequency values increase radially outward from the center:

$$F'_c(u, v) = F_c(u, v) \cdot (-1)^{x+y}, \quad c \in \{R, G, B\}. \quad (6)$$

Subsequently, the magnitude of the centered spectrum is computed for each channel:

$$M_c(u, v) = |F'_c(u, v)|, \quad c \in \{R, G, B\}. \quad (7)$$

Then, a logarithmic transformation with base b is applied to the magnitude:

$$L_c(u, v) = \log_b M_c(u, v), \quad c \in \{R, G, B\}, \quad (8)$$

where b is set as a hyperparameter. Finally, the transformed results of the three channels are combined into a single image, which is used as the input to the altitude estimation network. Denote the final frequency domain visualization image as $I_{in}^{\text{freq}}(u, v)$, defined by

$$I_{in}^{\text{freq}}(u, v) = [L_R(u, v), L_G(u, v), L_B(u, v)]. \quad (9)$$

We denote the entire preprocessing pipeline by the mapping Spat2Freq and therefore the overall process can be compactly written as

$$I_{in}^{\text{freq}} = \text{Spat2Freq}(I_{in}). \quad (10)$$

To this end, we obtain a RGB-visualized Fourier spectrum image, where the frequencies increase radially from the center

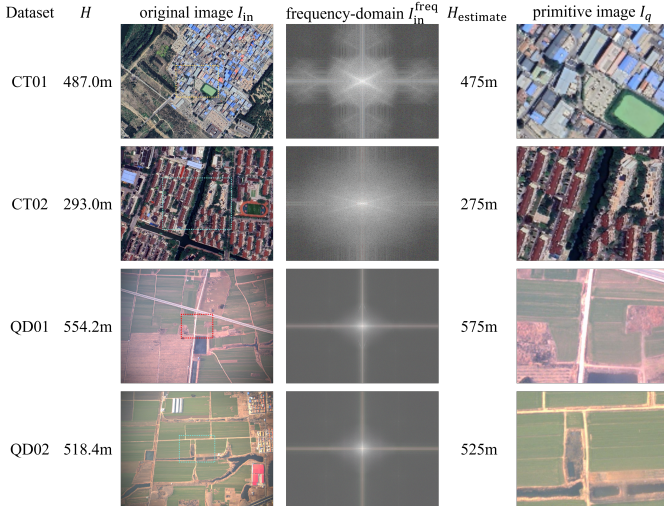


Fig. 2. *Schematic diagram of the processing procedure of the sample query images from 4 datasets. Among them, the frequency-domain I_{in}^{freq} have undergone brightness transformation for visual presentation effect.

and a logarithmic scaling is used to compress the dynamic range.

2) *Network Architecture*: The proposed network architecture consists of a backbone, an aggregator and a classifier. The backbone extracts the feature map of the original image and the aggregator obtains a feature vector containing the altitude information of the unmanned aerial vehicle through the feature map. Then a classifier is used to learn the prototype vectors representing classes of different altitude intervals. We divide the altitude range into cells, that are defined by a single hyper-parameter ΔH , representing the length of the cells' span in altitude. Each cell corresponds to a class. We denote the process of obtaining the altitude class set C_i from the frequency-domain input image I_{in}^{freq} via a neural network. Formally, this process is expressed as:

$$C_i = AC(I_{in}^{freq}). \quad (11)$$

3) *Altitude Class Division*: To enable altitude estimation, the flight altitude range $\{H \mid H_{\min} \leq H < H_{\max}\}$ is discretized into n equal intervals. Each interval I_i is defined as:

$$I_i = \{H \mid H_i \leq H < H_i + \Delta H\}, \quad i \in \{1, 2, \dots, n\}, \quad (12)$$

where the lower bound of the i -th interval, H_i , is given by:

$$H_i = H_{\min} + (i - 1)\Delta H.$$

Altitude estimation then reformulated as a classification problem, where the discretized intervals serve as distinct altitude classes. In particular, class C_i is defined as:

$$C_i = \left\{ H \mid \left\lceil \frac{H - H_{\min}}{\Delta H} \right\rceil + 1 = i \right\}. \quad (13)$$

For implementation, we set the interval size to $\Delta H = 50$ m. The set of altitude interval's center values is defined as:

$$\mathcal{H}_{\text{center}} = \{H_{\min} + (i - 0.5) \cdot \Delta H \mid i = 1, 2, \dots, n\}.$$

The mapping function from altitude class to estimated altitude, denoted as Class2Alt , is then given by:

$$\text{Class2Alt} : C_i \mapsto (H_{\min} + (i - 0.5) \cdot \Delta H). \quad (14)$$

To prevent blank-edge artifacts when normalizing image scale, we define H_{db} as the canonical relative altitude used to construct primitive map. Cropping is always performed from the high-altitude down to this reference altitude. Formally, we enforce

$$H_{\text{db}} \leq \min_i \mathcal{H}_{\text{center}}^{(i)},$$

where $\mathcal{H}_{\text{center}}^{(i)}$ denotes the estimated altitude of the i -th Class. To minimize the extent of cropping and maximize the retained field of view, we assign the primitive map's altitude to the lower bound. This configuration meets the blank-edge constraint while minimizing reduction in image coverage.

For altitude classification, we employ MixVPR [9], a robust architecture to extract global altitude-related features from frequency-domain-transformed images I_{in}^{freq} . The process of estimating relative altitude H_{estimate} from the raw image I_{in} can be reduced to the operator defined in eq. (1).

4) *Data Preparation*: During training, we fix the camera's intrinsic parameters such that, for any given altitude, the ground coverage can be computed. We then generate training samples by sampling remote-sensing imagery of the target area at uniform altitude intervals (e.g., every 5 m) and cropping each tile to match the computed ground coverage at that altitude. At inference time, if the deployed camera's intrinsic parameters differ from those used during offline training, the raw relative altitude estimate inferred by the pretrained model can be linearly scaled by the ratio between the deployed focal length and the one assumed during training.

B. VPR Module

1) *Primitive Image Collection*: Once the relative altitude estimation is obtained, the original onboard image can be cropped via the camera imaging model to obtain a **primitive image** by simulating a view at the canonical altitude H_{db} over the same UTM coordinates. The database is then organized as a collection of pre-rendered views at altitude H_{db} , and termed the **primitive map**. Aligning the query image with primitive map tiles built at a fixed altitude H_{db} normalizes scale variation and enables accurate geo-initialization on memory-constrained UAVs (see Fig. 3).

Let res_w and res_h denote the image resolution along the horizontal and vertical directions (in pixels), respectively, and let f_x and f_y represent the focal lengths in pixel units along the corresponding axes. Given the platform's relative altitude H , the physical dimensions of the ground area covered by the camera's field of view can be approximated by:

$$W_{\text{ground}} = \frac{res_w}{f_x} \cdot H, \quad H_{\text{ground}} = \frac{res_h}{f_y} \cdot H. \quad (15)$$

Here, W_{ground} and H_{ground} denote the physical width and height (in meters) of the ground area covered by the camera's field of view at relative altitude H , respectively. Under the pinhole camera model for downward-looking imaging, the airborne image is scaled and cropped around its original

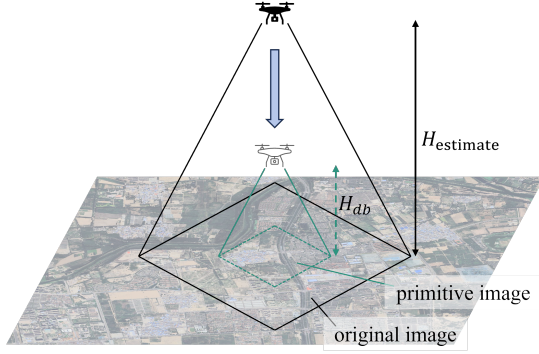


Fig. 3. The process to transform an input image to a primitive image.

center, ensuring that the center point remains unchanged. To compensate for scale differences caused by altitude variation and match the spatial extent of the corresponding primitive map, the original input airborne image I_{in} is first enlarged by a factor of $\frac{H_{estimate}}{H_{db}}$, then cropped to match its initial height and width. We denote the entire cropping-and-scaling pipeline by the function *Crop*, such that the resulting normalized query image is given by

$$I_q = \text{Crop}(I_{in}). \quad (16)$$

2) *Primitive Map Retrieval*: The overall VPR pipeline is illustrated in Fig. 4. To this end, we consider aerial VPR problem with known altitude. Note that the backend of the proposed relative altitude estimation module is designed as a universal module, seamlessly integrating with any VPR pipeline. In our framework, the primitive image, denoted by I_q , serves as the input to the VPR module. We represent a generic VPR pipeline as AVPR. Then, we retrieve the top $n_{retrieve}$ images, each characterized by a global feature vector and an associated geospatial coordinate. We denote the collection of these feature vectors by \mathcal{V} and aggregate the corresponding UTM coordinates into the set \mathcal{U} . Thus, we formalize the AVPR pipeline as a mapping from the input image to its retrieved references and their locations:

$$(\mathcal{V}, \mathcal{U}) = \text{AVPR}(I_q), \quad (17)$$

where \mathcal{V} is the set of top- $n_{retrieve}$ reference images and \mathcal{U} is the set of their corresponding UTM coordinates.

Given the significant advantages of classification-based VPR, as demonstrated in D&C [41], we adopt the *classify-then-retrieve* strategy. To facilitate efficient retrieval, we partition the remote sensing map into uniformly distributed square cells using UTM coordinates (*east*, *north*). Each cell has a side length of M , forming a set of non-overlapping partitions. These cells are treated as distinct classes, where each class is identified using an ID pair (e_i, n_j) . Formally, each class C_{e_i, n_j} is defined as:

$$C_{e_i, n_j} = \left\{ (\text{east}, \text{north}) : \left\lfloor \frac{\text{east}}{M} \right\rfloor = e_i, \quad \left\lfloor \frac{\text{north}}{M} \right\rfloor = n_j \right\}.$$

Consequently, the original primitive map database is divided into several independent sub-databases. The sub-database corresponding to each class is denoted by $DB_{e_i, n_j} \in \mathcal{D}$, and

the association between each class and its corresponding sub-database is defined by the function *Class2SubDB*:

$$\text{Class2SubDB} : C_{e_i, n_j} \mapsto DB_{e_i, n_j}. \quad (18)$$

We discretize the area into grid cells indexed by east-west coordinate e_i and north-south coordinate n_j , and denote the class of the (e_i, n_j) th cell by C_{e_i, n_j} . To minimize perceptual aliasing, we partition all classes into N^2 groups, each identified by a unique pair (u, v) :

$$G_{u, v} = \{ C_{e_i, n_j} \mid (e_i \bmod N = u) \wedge (n_j \bmod N = v) \}, \quad (19)$$

where N determines the minimum cell-unit separation between adjacent classes within the same group. Since each cell yields exactly one residue pair (u, v) , the resulting N^2 groups are mutually disjoint. Consequently, $|G| = N^2$. In order to obtain rotational robustness, images are augmented through rotations of 30° , forming the augmentation set $\alpha_{aug} = \{0, 30, \dots, 330\}$ for training.

Feature extraction is realized using the EfficientNet backbone [15], integrated with the aggregation module from MixVPR [9]. During inference, the top n_{class} are identified using Eq. (22), and the corresponding sub-databases are queried via the FAISS vector search library [11] to retrieve the top $n_{retrieve}$ global feature vectors. We set $n_{class} = 3$ and $n_{retrieve} = 10$ in our implementation.

C. Quality Adaptive Margin Classifier (QAMC)

Building on quality-adaptive margin loss (AdaFace) [69] to handle image quality variation, we introduce the *Quality Adaptive Margin Classifier* (QAMC), which retains discriminative prototypes for inference without increasing complexity. Unlike the original AdaFace, which solely relies on the embedding norm as a proxy for image quality, our QAMC further incorporates a sharpness-based indicator that explicitly measures the clarity of structural details in aerial images.

Formally, given an input image $I \in \mathbb{R}^{H \times W \times C}$, we first convert it to grayscale:

$$I_g(x, y) = \frac{1}{C} \sum_{c=1}^C I(x, y, c), \quad (x, y) \in [1, H] \times [1, W].$$

We then apply the Laplacian operator to obtain the edge response:

$$L(x, y) = \nabla^2 I_g(x, y) = \frac{\partial^2 I_g}{\partial x^2} + \frac{\partial^2 I_g}{\partial y^2}.$$

The sharpness score is defined as the variance of the Laplacian response:

$$Q_{\text{sharp}} = \text{Var}(L) = \frac{1}{HW} \sum_{x=1}^H \sum_{y=1}^W (L(x, y) - \bar{L})^2,$$

where \bar{L} is the mean of $L(x, y)$. A higher Q_{sharp} indicates richer texture and clearer structural details, while a lower value corresponds to blurred or low-quality imagery. We normalize Q_{sharp} and combine it with the embedding-norm-based quality estimate Q_{norm} to form a composite quality factor:

$$Q = \alpha \cdot Q_{\text{norm}} + (1 - \alpha) \cdot \hat{Q}_{\text{sharp}}, \quad \alpha \in [0, 1],$$

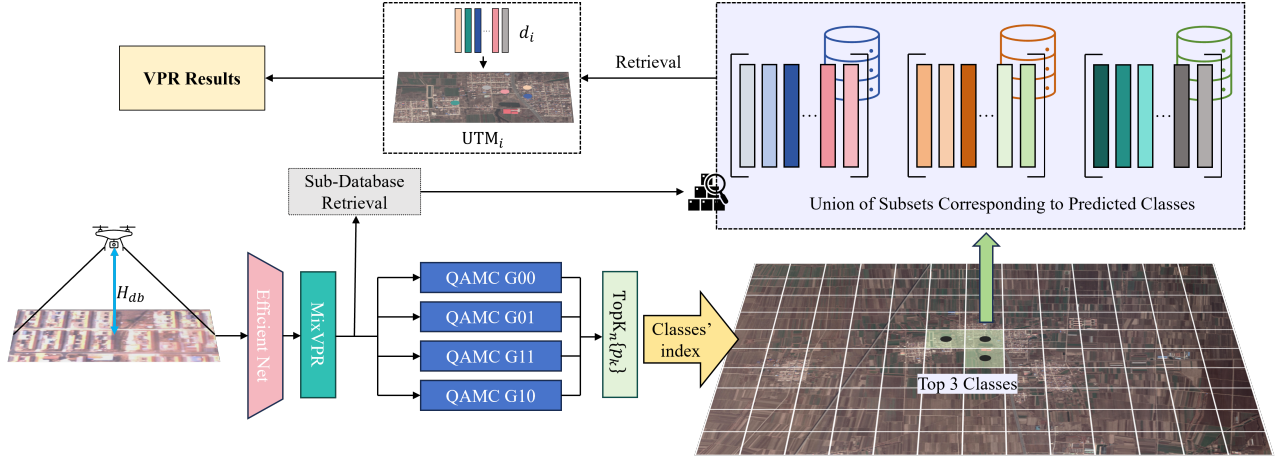


Fig. 4. VPR of the primitive images.

where \hat{Q}_{sharp} denotes the normalized sharpness score. This composite factor dynamically modulates the angular margin and scaling in the classification loss, enforcing stricter discriminative constraints on high-quality samples while relaxing the margin for blurred or low-quality inputs. This design adapts AdaFace’s quality-adaptive principle to the aerial VPR problem.

To further address the boundary confusion and enlarged label space caused by numerous densely distributed place-classes in large-scale VPR [39], [40], [70], we design a $|G|$ -way group-wise mixture-of-experts classifier that partitions spatially non-adjacent cells into separate groups. This joint design suppresses confusion between visually similar neighbors and enables efficient, fine-grained city-scale localization.

1) *Altitude classification*: The altitude classifier is represented by a prototype matrix $W_h \in \mathbb{R}^{n \times d_h}$, where n is the number of altitude classes and d_h is the dimensionality of the global embedding from the altitude backbone. Given a query embedding $x \in \mathbb{R}^{d_h}$, we compute

$$p_h(i) = [\text{softmax}(W_h^\top x)]_i, \quad i \in \{1, \dots, n\}, \quad (20)$$

where $p_h = (p_h(1), \dots, p_h(n))^\top \in \mathbb{R}^n$ is the vector of predicted class probabilities. We then map the output to its estimated altitude value:

$$\text{AltClassify} : \mathbb{R}^n \rightarrow \mathcal{H}_{\text{center}},$$

$$p_h \mapsto \text{Class2Alt} \left(\arg \max_{i \in \{1, \dots, n\}} p_h(i) \right). \quad (21)$$

2) *Place classification for VPR*: In the place classification branch, this composite quality factor is integrated into the group-wise mixture-of-experts classifier, ensuring that margin adaptation accounts not only for embedding magnitude but also for image sharpness, which is particularly critical in aerial VPR scenarios.

For the k -th group, the corresponding classifier uses a prototype matrix $W_k \in \mathbb{R}^{S_k \times d}$, where S_k is the number of classes in group k and d is the backbone embedding dimension. Given a test embedding $x \in \mathbb{R}^d$, we obtain group-wise predictions

$$p_k(c) = [\text{softmax}(W_k^\top x)]_c, \quad c \in \{1, \dots, S_k\},$$

where $p_k = (p_k(1), \dots, p_k(S_k))^\top \in \mathbb{R}^{S_k}$ is the score vector for group k . We then select the top n_{class} classes with the highest confidence across all groups. Let $\text{TopK}_{n_{\text{class}}} \{\cdot\}$ be the operator that extracts the top-ranked scores across all (k, c) pairs, yielding

$$\mathcal{C}_{\text{top}} = \text{TopK}_{n_{\text{class}}} \{ p_k(c) \}_{k \in \{1, \dots, |G|\}, c \in \{1, \dots, S_k\}}. \quad (22)$$

Each selected class $c \in \mathcal{C}_{\text{top}}$ is mapped to its corresponding sub-database via $\text{Class2SubDB}(c)$. The retrieval reference database is constructed as:

$$\begin{aligned} \text{CollectRetrievalDB} : \mathbb{R}^{S_1} \times \dots \times \mathbb{R}^{S_{|G|}} &\rightarrow \mathcal{D}, \\ \{p_k\}_{k=1}^{|G|} &\mapsto \bigcup \text{Class2SubDB}(\mathcal{C}_{\text{top}}), \end{aligned} \quad (23)$$

Let this union be the final reference database by $DB_{\text{retrieval}}$. Similarity search is then conducted within $DB_{\text{retrieval}}$ using the query’s global embedding, and the top n_{retrieve} results are finally obtained.

a) *Scalability Discussion*: The proposed VPR module adopts a grid-based classification with fixed cell sizes (e.g., 100 m) and shape. We emphasize that the spatial partition must be defined as a hyperparameter prior to training and inference, rather than being adaptively adjusted at runtime. This is because class labels are tied to specific spatial cells: if the boundaries were changed dynamically, the correspondence between training labels and inference labels would be lost, making the classifier inconsistent. Therefore, fixed discretization is necessary to ensure reproducibility and stable training.

We choose a cell size of 100 m because it matches the resolution of our database construction process. Reference tiles are cropped sequentially with a stride of about one third to one quarter of the tile edge, corresponding to a ground footprint shift of 60-70 m. Thus, 100 m provides a natural resolution for coarse localization or initialization: smaller cells would lead to excessive classes with insufficient samples, while larger cells would reduce estimation accuracy and increase scale mismatch.

Prior works have also relied on predefined spatial partitions, though with different strategies. For example, PlaNet [31] employs the S2 geometry library to partition the Earth into

hierarchical cells, and then adaptively merges or splits these cells according to the geographic density of training images. Thus, the resulting “adaptive cells” are irregular but fixed in boundary and distribution once defined, ensuring consistent labels during both training and inference. CPLaNet [37] employs combinatorial partitioning, HGE [36] adopts hierarchical coarse-to-fine grids, Divide & Classify [41] uses fixed UTM grids, and GeoCluster [58] applies clustering-based partitioning. These methods demonstrate that spatial boundaries must be set in advance, either uniformly or adaptively, to enable classification-based localization. In our case, the fixed 100m grid is effective for the experimental regions, while scalability to larger deployments can be achieved by adopting hierarchical classification, adaptive grid sizes, clustering-based partitioning, or multi-scale retrieval pipelines.

IV. EXPERIMENTS

A. Dataset

Since there are no publicly available datasets addressing the large-scale, high-altitude localization problem, we have designed two synthetic datasets (CT01 and CT02) and collected two real-world datasets (QD01 and QD02) using UAV-acquired top-down imagery in rural areas of Qingdao, China.

TABLE I
SENSORS’ DETAILED SPECIFICATIONS AND PARAMETERS

Sensor	Details
Camera	Type: FLIR BFS-U3-31S4C-C RGB channels, 2048 × 1536 resolution, 55Hz max frame rate (20Hz in experiment), global shutter
Lens	Type: Chiopt FA0401C 82.9° horizontal FOV, 66.5° vertical FOV, 4~75 mm focal length
GNSS	Type: NovAtel OEM718D Dual-antenna, 5 Hz update, 1.5 m (RMS) with single point, 1cm + 1ppm (RMS) with RTK
Altimeter	Type: Benewake TF350 10Hz update, 350m maximum detection range with 0.1m accuracy

CT01 and CT02 datasets are synthetic datasets and are generated by cropping remote sensing maps. Specifically, we acquired up-to-date remote sensing maps over regions of approximately 45 km² in the outskirts of Beijing and the urban area of Shanghai, respectively. The altitude range was set between 100m and 700m, and for each region 500 groups of UTM and altitude values were generated randomly. The remote sensing maps were then cropped according to the onboard camera parameters, and two types of degradation were added to better approximate UAV-acquired imagery: Gaussian noise to simulate sensor noise, JPEG compression artifacts to mimic transmission and storage losses. The VPR network is trained using historical remote sensing maps from the respective regions, with the search areas for CT01 and CT02 with the size of 7.8 × 5.9 km and 8.8 × 4.9 km, respectively.

For self-collected datasets, the detailed specifications and parameters of the data acquisition sensor mounted on the

UAV platform are presented in Table I. The onboard camera captures images at a resolution of 2048 × 1536 pixels, with a focal length of $f = 1200$ pixels. The flight dataset (QD01 and QD02) were collected in the area of Jimo District and Chengyang District in Qingdao. In these datasets, the ground predominantly consists of farmland, which poses a considerably greater challenge compared to urban and suburban areas. The number of test images in QD01 and QD02 are 814 and 470, respectively. The altitude range is set between 100 m and 700 m. The search areas for QD01 and QD02 are identical, each covering 4.8 × 3.5 km. Detailed information on the test datasets is provided in Table II.

B. Experimental Setup

1) *Hyperparameter choices:* We set the altitude interval $\Delta H = 50$ m to balance estimation precision and class granularity. Smaller intervals would result in an excessive number of altitude classes with insufficient samples per class, increasing training difficulty and overfitting risk. Conversely, larger intervals reduce altitude estimation resolution and introduce scale mismatch during cropping. The fixed setting $\Delta H = 50$ m is used in our main experiments as it offers a good balance between estimation accuracy and class stability, as confirmed by the comparative results in Table VII. A detailed analysis of this trade-off and the effectiveness of adaptive binning strategies is provided in Section *Altitude Interval Size*.

For place classification, we adopt a grid size of $M = 100$ m, consistent with our database construction process. Reference tiles are cropped sequentially with a stride of approximately one third to one quarter of the tile edge, corresponding to a ground footprint shift of 60-70m. This stride defines the effective spatial resolution of the database, meaning that any localization based on tile-level retrieval cannot be more precise than the tile spacing itself (i.e., 60-70m). This resolution reflects the granularity of our reference map: retrieval can only localize a query to the nearest tile, so the tile spacing directly determines the upper bound of VPR precision. Therefore, $M = 100$ m provides a natural setting for coarse localization or initialization. Finer localization can be achieved in subsequent stages via local feature matching, geometric verification, or homography estimation. Finally, following the Divide & Classify strategy [41], we partition the spatial domain into $N = 2$ groups. This reduces the number of classes per classifier, alleviates boundary ambiguity, and improves discriminability. Group-wise classification reduces intra-class variance and improves feature separability, especially when the spatial domain exhibits heterogeneous appearance distributions. Such strategies have been shown to enhance performance in prior city-scale VPR studies, such as Divide & Classify [41] and GeoVINS [60], and we find them similarly beneficial in both rural and semi-urban environments.

2) *Implementation details:* In the altitude estimation module, we can get the altitude interval ΔH using eq. (12). For example, choosing $H_{\min} = 100$ m, $H_{\max} = 700$ m, $\Delta H = 50$ m and sampling interval $\delta H = 5$ m yields $N = (H_{\max} - H_{\min})/\Delta H = 12$ discrete altitude classes with reference altitudes $h_k = \{100, 105, 110, \dots, 695\}$.

TABLE II
DETAILS OF THE TEST DATA ACQUISITION

Datasets	Region	Acquisition Method	Number of Test Images	the Size of Search Area	Altitude Range
CT01	Beijing	Cropped remote sensing map with degradation	500	7.8×5.9 km	100m-700m
CT02	Shanghai	Cropped remote sensing map with degradation	500	8.8×4.9 km	100m-700m
QD01	Qingdao	UAV real-flight	814	4.8×3.5 km	100m-650m
QD02	Qingdao	UAV real-flight	470	4.8×3.5 km	100m-650m

For training, we use the Adam optimizer and ReduceLROn-Plateau as the learning rate scheduler. The initial learning rate for the deep feature extraction network is set to 1×10^{-4} , while the classifier’s learning rate is set to 1×10^{-2} . The patience parameter is set to 10, meaning that if the training loss does not improve within 10 epochs, the learning rate is adjusted accordingly. The classifier parameters are configured with $m = 0.2$ and $s = 100$. In the Spat2Freq module, we set the nonlinear mapping parameter to be $b = 1.5$. We adopt a cropped ResNet50 as the backbone feature extractor, truncating the fourth layer of ResNet and employing MixVPR as the aggregator. During training, we apply color jittering to the images to ensure robustness to varying illumination conditions.

In the VPR module, we set the grid cell size to be $M = 100$ m and the grouping parameter to be $N = 2$, partitioning the space into four groups ($|G| = 4$). The classifier and learning rate settings are the same with those in the altitude classification module. During training, the ground-plane footprint of each image is computed using eq. (15) with the altitude parameter being $h = 125$ m. The feature extraction backbone is EfficientNet B5, combined with MixVPR for aggregation.

3) *Metrics*: For altitude estimation, we consider the mean altitude estimation error E_{avg} and the percentage of estimates with error below a threshold D , denoted as $P_{E < D}$. In VPR evaluation, we measure performance using the standard retrieval recall at rank N (R@N), which quantifies the proportion of queries for which at least one correctly matched reference image appears among the top- N retrieved candidates. Specifically, we use R@1 and R@5 as evaluation criteria. Once the initial localization coordinates are obtained, we compute the average estimation error d_{avg} by measuring the distance between the estimated UTM coordinates and the ground-truth UTM coordinates. The threshold is considered 100m, which means that if the estimated UTM coordinates are within 100 m with respect to the ground truth, the localization is considered successful.

4) *Baselines and References*: To ensure fair comparisons, all classification methods are evaluated with identical batch sizes, data augmentation strategies, backbone architectures, and training datasets.

a) *Altitude Estimation References*: In UAV applications, relative altitude ground truth is typically obtained via non-visual sources such as barometric sensors, altimeter readings, or DEM alignment. These methods are used in our datasets to generate altitude annotations, but they rely on external data and hardware, and thus cannot serve as baselines for evaluating

vision-only approaches.

To date, no vision-only baseline exists for single-image relative altitude estimation from nadir-view aerial imagery. Therefore, we include monocular metric depth estimation (MMDE) methods only as contextual references. Among existing vision-based techniques, MMDE models such as Depth Anything V2 and UniDepth V2 are the closest in spirit to our task, as they infer geometric quantities from a single image. However, they are designed for dense pixel-wise depth prediction within limited ranges, not for global altitude estimation. For reference, we apply Depth Anything V2 [61] and UniDepth V2 [62], and compute the mean value of the predicted depth map as the estimated relative altitude. These results are reported only for contextual comparison, not as baselines, and help highlight the differences in task formulation and the advantages of the proposed method.

b) *VPR Baselines*: For VPR comparison, we evaluate MixVPR [9], CosPlace [39], CricaVPR [20], and DINOv2-SALAD [21] as baseline models. MixVPR and CosPlace utilize CNN-based feature extraction networks, while CricaVPR and DINOv2-SALAD rely on DINOv2 [19] networks.

C. Main Results

We first present VPR results and demonstrate the plug-and-play capability of the proposed altitude estimation approach. The results are given in Table III. We observe that incorporating relative altitude estimation yields substantial improvements in performance across different backbone architectures. When averaged over all datasets, Recall@1 (R@1) shows improvements of 40.84, 27.47, 20.95, 21.95, and 38.04 percent for MixVPR, CosPlace, SALAD, CricaVPR, and our VPR module, respectively. Similarly, Recall@5 (R@5) shows improvements of 54.89, 40.62, 40.56, 39.50, and 60.29 percentage points, respectively. These results clearly demonstrate that the relative altitude estimation plays a significant role in improving image retrieval performance.

D. Real-Time Performance

To evaluate the computational efficiency of the proposed framework, we conducted runtime analysis on a workstation equipped with a single NVIDIA GeForce RTX 4090 GPU, an AMD EPYC 7352 CPU with 11 vCPUs. Table IV reports the average and maximum latency, peak CPU/GPU memory usage, and overall throughput in frames per second (FPS) for each module: relative altitude estimation (RAE), altitude-aware cropping (Crop), VPR classification (VPR (C)), and VPR retrieval (VPR (R)).

TABLE III
RESULTS USING DIFFERENT VPR METHOD WITH OR WITHOUT RELATIVE ALTITUDE ESTIMATION(RAE)

VPR Method	RAE	CT01		CT02		QD01		QD02	
		R@1↑	R@5↑	R@1↑	R@5↑	R@1↑	R@5↑	R@1↑	R@5↑
MixVPR	✓	63.80	87.80	62.20	80.00	32.80	60.69	<u>46.81</u>	<u>57.87</u>
	✗	16.40	16.80	15.40	16.60	16.40	16.80	15.40	16.60
CosPlace	✓	50.40	67.00	44.80	59.00	32.80	46.93	30.00	44.26
	✗	14.20	15.00	16.00	16.80	16.22	18.67	1.70	4.26
SALAD	✓	60.70	<u>95.20</u>	<u>64.40</u>	<u>88.60</u>	<u>53.62</u>	<u>75.80</u>	45.32	<u>66.53</u>
	✗	29.80	32.60	26.80	31.00	43.00	49.02	40.64	51.28
CricaVPR	✓	<u>66.40</u>	87.60	56.80	75.60	53.07	<u>75.80</u>	36.17	61.49
	✗	21.80	22.80	18.20	19.20	46.56	52.21	38.09	48.30
Our VPR Module	✓	77.20	97.20	68.40	90.80	54.67	78.01	47.45	67.23
	✗	26.80	29.20	24.60	26.80	19.04	24.82	25.11	11.28

The results show that RAE and cropping are lightweight, with average latencies of 10.7 ms and 12.4 ms, respectively. The classification stage is the most computationally demanding, averaging 50.6 ms per query, while retrieval over candidate classes adds only 1.5 ms. Peak GPU memory usage remains below 600 MB for all modules, and CPU memory consumption is modest, with incremental usage under 100 MB per stage. End-to-end throughput reaches 13.3 FPS, which satisfies real-time requirements for UAV applications operating at typical video frame rates (10-15 Hz). These results confirm that the proposed pipeline is computationally efficient and suitable for deployment on airborne platforms.

TABLE IV
*REAL-TIME PERFORMANCE

	RAE	Crop	VPR (C)	VPR (R)
Avg latency (ms)	10.7	12.4	50.6	1.5
Max latency (ms)	14.0	36.5	92.7	4.0
Peak CPU ABS (MB)	260.57	679.81	1830.71	1830.74
CPU DELTA (MB)	0.48	21.09	70.45	2.74
Peak GPU (MB)	54.77	0.00	574.67	429.36
FPS (Frames Per Second)	13.3			

E. Ablation Study

1) *Image Pre-processing*: To demonstrate the usefulness of the proposed Spat2Freq image pre-processing process for relative altitude estimation problem, we conduct experiments comparing the performance of models trained on Spat2Freq-processed images with those trained directly on spatial-domain images. Table V summarizes the average altitude estimation error and classification accuracy under two configurations: with and without Spat2Freq. Figure 5 provides a visual comparison of the estimated relative altitudes across four datasets (CT01, CT02, QD01, QD02), highlighting the performance improvement introduced by Spat2Freq. In each subfigure, every point represents a single query image, with the true relative altitude on the horizontal axis and the estimated relative altitude on the vertical axis. Green points correspond to models trained without Spat2Freq, while blue points correspond to models trained with Spat2Freq. The yellow diagonal line indicates perfect estimation, i.e., cases where H_{estimate} equals

the ground-truth relative altitude. Three pairs of symmetrically placed dashed lines represent error thresholds of ± 25 m (purple), ± 50 m (red), and ± 100 m (dark blue), respectively. It is evident that the model trained with Spat2Freq achieves superior estimation accuracy, as indicated by its outputs being more concentrated near the yellow line and more frequently residing within the defined error thresholds.

2) *Classifier*: We next conduct experiments on the role of the classifiers utilizing different loss functions, specifically: (1) a standard fully connected classifier trained with cross-entropy loss (CE), (2) the Additive Angular Margin Classifier (AAMC) trained with ArcFace Loss, and (3) the Quality Adaptive Margin Classifier (QAMC) trained with AdaFace Loss. We integrate these classifiers within the VPR pipeline and evaluate the impact of each loss function on retrieval performance. The results are shown in Table VI. It is evident that the proposed QAMC, by leveraging an adaptive strategy, performs best among VPR systems built upon a classification-then-retrieval framework.

3) *Altitude Interval Size*: We further analyze the impact of altitude interval size ΔH on relative altitude estimation and downstream VPR problems. As shown in Table VII, fixed intervals exhibit a clear trade-off: smaller bins (e.g., 25 m) improve fine-grained accuracy at tight thresholds ($P_{E<25}$, $P_{E<50}$) but suffer from enlarged class sets and reduced per-class samples, leading to unstable retrieval. Conversely, coarse bins (e.g., 100 m) simplify training but degrade estimation accuracy (E_{avg}) and retrieval performance due to mismatched cropping ratios. Intermediate settings (50-75 m) achieve more balanced results, with $\Delta H = 50$ often yielding the best compromise between estimation error and retrieval recall.

To overcome the inherent nonlinearity between altitude and cropping ratio, we design a variable-interval strategy based on an exponential function. Specifically, we set $H_0 = 100$ m as the starting altitude, $\Delta_0 = 20$ m as the base interval, and $r = 1.1$ as the growth rate. The lower bound of the i -th interval is defined by the cumulative geometric progression

$$H_i = H_0 + \Delta_0 \cdot \frac{r^i - 1}{r - 1}, \quad i \in \mathbb{Z}_{\geq 0},$$

and the corresponding interval is $I_i = \{H \mid H_i \leq H < H_{i+1}\}$. Given an input altitude H (for a sample indexed by

TABLE V
RELATIVE ALTITUDE ESTIMATION WITH AND WITHOUT Spat2Freq

Spat2Freq	CT01				CT02			
	$E_{avg} \downarrow$	$P_{E<25} \uparrow$	$P_{E<50} \uparrow$	$P_{E<100} \uparrow$	$E_{avg} \downarrow$	$P_{E<25} \uparrow$	$P_{E<50} \uparrow$	$P_{E<100} \uparrow$
✓	17.75	79.80	97.80	99.60	21.10	74.40	95.40	99.00
✗	29.33	62.00	83.60	95.60	25.99	60.40	85.20	98.80

Spat2Freq	QD01				QD02			
	$E_{avg} \downarrow$	$P_{E<25} \uparrow$	$P_{E<50} \uparrow$	$P_{E<100} \uparrow$	$E_{avg} \downarrow$	$P_{E<25} \uparrow$	$P_{E<50} \uparrow$	$P_{E<100} \uparrow$
✓	59.42	43.00	67.74	78.75	47.96	47.45	74.04	84.68
✗	73.35	39.80	56.63	75.43	60.97	31.91	60.00	82.34

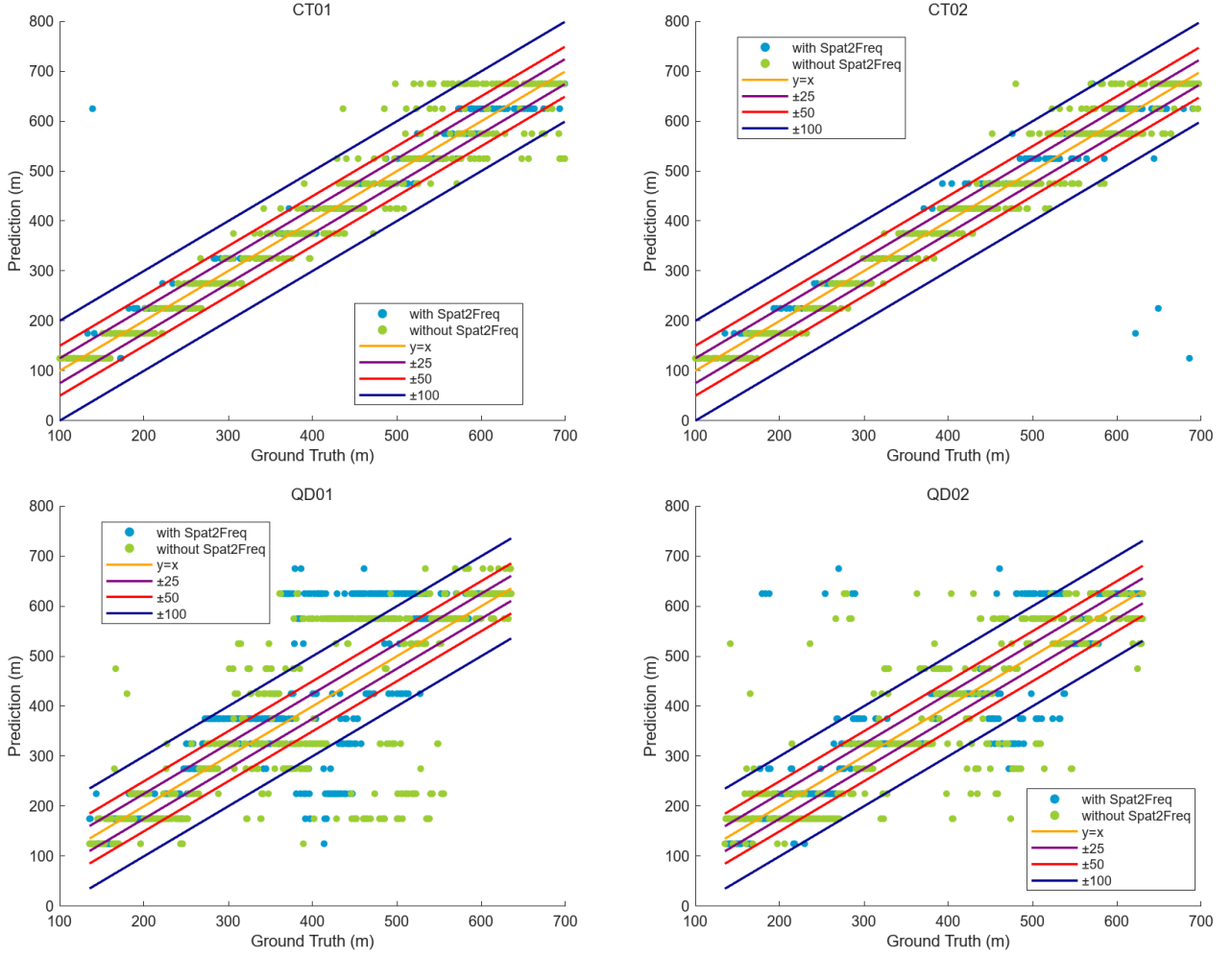


Fig. 5. Relative Altitude Estimation Results

TABLE VI
RESULTS USING DIFFERENT CLASSIFIERS

Method	CT01		CT02		QD01		QD02	
	R@1↑	R@5↑	R@1↑	R@5↑	R@1↑	R@5↑	R@1↑	R@5↑
QAMC	77.60	98.20	71.20	93.60	55.46	81.08	51.55	74.89
AAMC	72.00	93.20	73.00	93.00	51.74	74.45	50.55	68.09
CE	68.80	92.60	63.80	84.20	50.61	75.92	52.13	71.28

i), the class index C_i induced by the exponential binning rule is

$$C_i = \left\lfloor \log_r \left(1 + \frac{(H - H_0)(r - 1)}{\Delta_0} \right) \right\rfloor,$$

TABLE VII
*COMPARISON BETWEEN DIFFERENT ALTITUDE INTERVAL

ΔH	CT01						CT02					
	E_{avg}	$P_{E<25}$	$P_{E<50}$	$P_{E<100}$	R@1	R@5	E_{avg}	$P_{E<25}$	$P_{E<50}$	$P_{E<100}$	R@1	R@5
25	20.35	69.40	91.40	99.60	77.60	98.20	22.50	65.40	89.80	100.00	61.40	<u>92.60</u>
50	17.75	79.80	97.80	100.00	77.20	97.20	<u>21.10</u>	74.40	95.40	99.00	68.40	90.80
75	24.69	54.80	92.00	<u>99.80</u>	79.00	<u>97.80</u>	24.98	58.00	90.20	99.20	<u>68.00</u>	86.80
100	27.81	47.60	88.60	<u>99.80</u>	64.00	90.20	29.19	45.20	85.40	<u>99.60</u>	56.80	80.60
Variable	<u>18.90</u>	<u>73.00</u>	<u>94.00</u>	100.00	<u>78.40</u>	98.20	18.95	<u>69.80</u>	<u>93.40</u>	100.00	68.40	93.60

ΔH	QD01						QD02					
	E_{avg}	$P_{E<25}$	$P_{E<50}$	$P_{E<100}$	R@1	R@5	E_{avg}	$P_{E<25}$	$P_{E<50}$	$P_{E<100}$	R@1	R@5
25	47.06	<u>38.33</u>	<u>59.09</u>	86.49	52.95	72.97	52.47	25.53	52.98	<u>90.43</u>	51.06	65.96
50	59.42	43.00	64.74	78.75	<u>54.67</u>	78.01	<u>47.96</u>	47.45	74.04	84.68	47.45	<u>67.23</u>
75	58.57	28.01	47.42	<u>83.29</u>	43.98	59.58	61.43	28.94	56.60	86.17	40.43	67.02
100	93.92	36.86	56.02	71.01	48.28	61.06	58.35	<u>34.89</u>	<u>62.55</u>	84.89	42.13	71.06
Variable	<u>57.31</u>	34.40	53.32	78.99	56.76	<u>74.08</u>	46.18	32.98	57.66	92.34	51.49	65.96

which assigns H to its interval via the inverse of the cumulative spacing. The set of class-center altitudes associated with these intervals is

$$\mathcal{H}_{\text{center}} = \left\{ H_0 + \Delta_0 \cdot \frac{r^k - 1}{r - 1} \mid k \in \mathbb{Z}_{\geq 0} \right\},$$

and the corresponding mapping from class index to its center altitude is

$$\text{Class2Alt} : C_i \mapsto H_0 + \Delta_0 \cdot \frac{r^{C_i} - 1}{r - 1}.$$

Together, these expressions ensure that each altitude bin corresponds to a nearly uniform change in cropping ratio: finer bins are allocated at lower altitudes where frequency-domain cues are more sensitive to scale, while coarser bins are allocated at higher altitudes where the relative change in image scale diminishes.

The results in Table VII verify the effectiveness of the proposed adaptive binning strategy. Across all datasets, the altitude interval size ΔH plays a critical role in balancing estimation precision and retrieval robustness. Fixed intervals offer predictable behavior but suffer from either over-fragmentation (e.g., small ΔH leading to sparse class samples) or excessive coarseness (e.g., large ΔH causing scale mismatch). In contrast, the exponential binning strategy improves performance by matching bin granularity to scale sensitivity, reducing low-altitude ambiguity and high-altitude distortion for more accurate estimation and robust VPR.

4) *Relative Altitude Estimation*: To further evaluate the performance of the proposed relative estimation module, we conduct a comparative analysis with other state-of-the-art monocular metric depth estimation methods, i.e., Depth Anything V2 and UniDepth V2. The results are shown in Table VIII.

Since MMDE algorithms produce dense depth maps, we compute the arithmetic mean of all elements in the dense estimation matrix to represent the value of relative altitude. Experimental results indicate that while traditional MMDE methods struggle to yield accurate estimates, the dedicated altitude estimation module achieves a noteworthy level of accuracy on relative altitude estimation.

In our experiments, we evaluated the performance of our method compared to two state-of-the-art approaches (UniDepth V2 and Depth Anything V2) by computing the average metrics for each of four datasets (CT01, CT02, QD01, and QD02). For a given metric — whether the average error E_{avg} , Recall@1 (R@1), or Recall@5 (R@5) — we defined the baseline as the mean value obtained by UniDepth V2 and Depth Anything V2, and quantified the improvement as our method’s score minus this baseline. Specifically, for E_{avg} , the reductions were 258.91 units for CT01, 272.85 for CT02, 130.13 for QD01, and 146.47 for QD02, resulting in an average decrease of approximately 202.1 units. Similarly, for R@1, our method exceeded the baseline by 48.70 percentage on CT01, 43.30 on CT02, 16.46 on QD01, and 17.24 on QD02, with an average gain of about 31.4 percent. For R@5, the gains were even more pronounced, at 66.40, 63.40, 26.59, and 19.47 percent for CT01, CT02, QD01, and QD02, respectively, corresponding to an overall increase of approximately 44 percent. These results demonstrate that our approach substantially reduces localization error while significantly improving both strict and relaxed recall metrics, thereby confirming its superiority in error control and matching accuracy across diverse evaluation scenarios.

Note that these MMDE models are not designed for altitude estimation; their results are reported as contextual references to illustrate the gap between dense depth prediction and our dedicated altitude estimation module.

5) *Localization Refinement with Weighted Coordinate Estimation (WCE) and Outlier Filtering*: We propose a method to estimate the UTM coordinate $\text{UTM}^* = (\text{UTM}e^*, \text{UTM}n^*)$ and refine the localization result of a query image based on the retrieval results from VPR, incorporating a Support Vector Machine (SVM)-based outlier filtering strategy. Let $d_q \in \mathbb{R}^C$ denote the global feature vector of the query image. From the retrieval process, the top n_{retrieve} reference images are obtained, each associated with a global feature vector and a corresponding UTM coordinate. Denote the set of retrieved global features by

$$\mathcal{V} = \{d_i \in \mathbb{R}^C \mid i = 1, 2, \dots, n_{\text{retrieve}}\},$$

TABLE VIII
COMPARISON WITH MMDE CONTEXT REFERENCES

Method	CT01						CT02					
	E_{avg}	$P_{E<25}$	$P_{E<50}$	$P_{E<100}$	R@1	R@5	E_{avg}	$P_{E<25}$	$P_{E<50}$	$P_{E<100}$	R@1	R@5
UniDepth V2	271.61	0.80	2.00	13.60	30.20	32.40	288.64	1.00	2.00	13.80	25.40	27.80
Depth Anything V2	281.70	6.20	11.00	18.80	26.80	29.20	299.25	6.40	9.40	21.00	24.80	27.00
Ours	17.75	79.80	97.80	100.00	77.20	97.20	21.10	74.40	95.40	99.00	68.40	90.80

Method	QD01						QD02					
	E_{avg}	$P_{E<25}$	$P_{E<50}$	$P_{E<100}$	R@1	R@5	E_{avg}	$P_{E<25}$	$P_{E<50}$	$P_{E<100}$	R@1	R@5
UniDepth V2	174.91	0.00	1.23	26.90	39.68	59.83	179.10	0.00	1.49	13.83	47.23	67.87
Depth Anything V2	239.92	1.23	20.02	28.38	19.04	25.31	264.17	3.83	10.85	18.09	13.19	27.66
Ours	59.42	43.00	64.74	78.75	54.67	78.01	47.96	47.45	74.04	84.68	47.45	67.23

- MMDE models are not designed for altitude estimation; they are included as context references only.

and the corresponding UTM coordinate set by

$$\mathcal{U} = \{\text{UTM}_i = (\text{UTM}_{e_i}, \text{UTM}_{n_i}) \mid i = 1, 2, \dots, n_{\text{retrieve}}\}.$$

To filter unreliable localization candidates, One-Class SVM is trained on \mathcal{U} using kernel K . The resulting decision function is

$$f_{\text{oc}}(u) = w \cdot \phi(u) - \rho,$$

where $\phi(u)$ denotes the kernel feature map, w the learned hyperplane weight, and ρ the decision offset. The filtered UTM coordinate set is then defined by

$$\mathcal{U}_{\text{filtered}} = \{u_i \in \mathcal{U} \mid f_{\text{oc}}(u_i) \geq 0\},$$

with inliers retained and outliers discarded. For brevity, this filtering is denoted as

$$\mathcal{U}_{\text{filtered}} = \text{SVM}_{\text{oc}}(\mathcal{U}).$$

The corresponding filtered global feature set is

$$\mathcal{V}_{\text{filtered}} = \{d_i \in \mathcal{V} \mid \text{UTM}_i \in \mathcal{U}_{\text{filtered}}\}.$$

To compute the final localization estimate, each filtered feature vector is assigned a weight inversely proportional to its Euclidean distance from the query vector:

$$w_i = \frac{1}{\|d_q - d_i\|_2}, \quad \text{for } d_i \in \mathcal{V}_{\text{filtered}}.$$

These weights are then normalized:

$$w_i^* = \frac{w_i}{\sum_j w_j}, \quad i = 1, 2, \dots, n_{\text{retrieve}}.$$

The estimated UTM coordinate is computed as a weighted average:

$$\text{UTM}^* = \sum_i w_i^* \cdot \text{UTM}_i,$$

where UTM^* denotes the final predicted location.

We refer this process as Weighted Coordinate Estimation (WCE), which computes UTM^* from the retrieved global feature set \mathcal{V} and the corresponding coordinate set \mathcal{U} , formally expressed as

$$\text{UTM}^* = \text{WCE}(\mathcal{V}, \mathcal{U}).$$

Table IX compares the localization accuracy between the baseline and WCE-enhanced approaches. The reported metric

TABLE IX
 S_{Loc} COMPARISON WITH AND WITHOUT WCE

WCE	CT01	CT02	QD01	QD02
✓	96.20	87.00	69.78	59.57
✗	77.20	68.40	54.67	47.45

is the localization success rate, S_{Loc} , which is defined as the proportion of test images whose estimated UTM coordinate lies within 100 meters of the ground-truth location. Formally,

$$S_{\text{Loc}} = \frac{N_{\text{success}}}{N_{\text{total}}} \times 100\%,$$

where N_{success} denotes the number of successful queries, and N_{total} is the total number of evaluated queries.

Under this criterion, localization success (S_{Loc}) is defined as the proportion of query images whose estimated UTM coordinates fall within 100m of the ground truth. Table IX shows that, across all datasets, S_{Loc} is consistently higher with WCE than without it. This indicates that aggregating multiple retrieved candidates with distance-based weighting and One-Class SVM outlier filtering improves robustness to noisy matches and translates into higher-precision localization.

V. CONCLUSION

In this paper, we introduce an altitude-adaptive visual place recognition (VPR) framework for airborne platforms. We exploit frequency-domain processing to capture subtle patterns in ground textures caused by altitude changes. We cast relative altitude estimation problem as a classification task by discretizing flight altitudes into intervals and learning representative prototypes for each interval, yielding robust altitude estimations and facilitating integration with the VPR task. We also propose an altitude-based image cropping mechanism that normalizes variable-scale images to a fixed-scale reference map, guaranteeing consistent feature alignment. Extensive experiments in diverse terrains and altitude conditions show that our method achieves high place-recognition success rate and reliable pose estimation using only visual input. To the best of our knowledge, this is the first work that estimates relative altitude from a single nadir image without using auxiliary sensors or relying on multi-view constraints, providing a

vision-only solution for altitude-aware VPR. This work shows that task-driven combinations of simple operations can yield a novel and effective solution, establishing the first vision-only single-image altitude estimator for airborne platforms.

For future work, we plan to develop a unified backbone network with task-specific adapters for both altitude estimation and place recognition. By sharing a common feature extractor while maintaining separate heads for each task, we aim to further streamline the pipeline and improve modularity under varying altitude conditions.

REFERENCES

- [1] H. Jégou, F. Perronnin, M. Douze, J. Sánchez, P. Pérez, and C. Schmid, “Aggregating Local Image Descriptors into Compact Codes,” *IEEE Transactions on Pattern Analysis and Machine Intelligence*, vol. 34, no. 9, pp. 1704–1716, Sep. 2012.
- [2] H. Jégou and A. Zisserman, “Triangulation Embedding and Democratic Aggregation for Image Search,” in *2014 IEEE Conference on Computer Vision and Pattern Recognition*, Jun. 2014, pp. 3310–3317, iISSN: 1063-6919.
- [3] F. Perronnin, Y. Liu, J. Sánchez, and H. Poirier, “Large-scale image retrieval with compressed Fisher vectors,” in *2010 IEEE Computer Society Conference on Computer Vision and Pattern Recognition*, Jun. 2010, pp. 3384–3391, iISSN: 1063-6919.
- [4] M. Zaffar, S. Ehsan, M. Milford, and K. McDonald-Maier, “CoHOG: A Light-Weight, Compute-Efficient, and Training-Free Visual Place Recognition Technique for Changing Environments,” *IEEE Robotics and Automation Letters*, vol. 5, no. 2, pp. 1835–1842, Apr. 2020.
- [5] R. Arandjelovic, P. Gronat, A. Torii, T. Pajdla, and J. Sivic, “NetVLAD: CNN Architecture for Weakly Supervised Place Recognition,” *IEEE Transactions on Pattern Analysis and Machine Intelligence*, vol. 40, no. 6, pp. 1437–1451, Jun. 2018.
- [6] H. J. Kim, E. Dunn, and J.-M. Frahm, “Learned Contextual Feature Reweighting for Image Geo-Localization,” in *2017 IEEE Conference on Computer Vision and Pattern Recognition (CVPR)*. Honolulu, HI: IEEE, Jul. 2017, pp. 3251–3260, iISSN: 1063-6919.
- [7] L. Liu, H. Li, and Y. Dai, “Stochastic Attraction-Repulsion Embedding for Large Scale Image Localization,” in *2019 IEEE/CVF International Conference on Computer Vision (ICCV)*. Seoul, Korea (South): IEEE, Oct. 2019, pp. 2570–2579, iISSN: 2380-7504.
- [8] M. Zaffar, S. Garg, M. Milford, J. Kooij, D. Flynn, K. McDonald-Maier, and S. Ehsan, “VPR-Bench: An Open-Source Visual Place Recognition Evaluation Framework with Quantifiable Viewpoint and Appearance Change,” *International Journal of Computer Vision*, vol. 129, no. 7, pp. 2136–2174, Jul. 2021.
- [9] A. Ali-Bey, B. Chaib-Draa, and P. Giguere, “MixVPR: Feature Mixing for Visual Place Recognition,” in *2023 IEEE/CVF Winter Conference on Applications of Computer Vision (WACV)*. Waikoloa, HI, USA: IEEE, Jan. 2023, pp. 2997–3006.
- [10] A. Ali-bey, B. Chaib-draa, and P. Giguère, “BoQ: A Place is Worth a Bag of Learnable Queries,” in *2024 IEEE/CVF Conference on Computer Vision and Pattern Recognition (CVPR)*. Seattle, WA, USA: IEEE, Jun. 2024, pp. 17 794–17 803, iISSN: 2575-7075.
- [11] J. Johnson, M. Douze, and H. Jegou, “Billion-Scale Similarity Search with GPUs,” *IEEE Transactions on Big Data*, vol. 7, no. 3, pp. 535–547, Jul. 2021.
- [12] M. Douze, A. Guzhva, C. Deng, J. Johnson, G. Szilvasy, P.-E. Mazaré, M. Lomeli, L. Hosseini, and H. Jégou, “The Faiss library,” Feb. 2025, arXiv:2401.08281 [cs].
- [13] K. He, X. Zhang, S. Ren, and J. Sun, “Deep Residual Learning for Image Recognition,” in *2016 IEEE Conference on Computer Vision and Pattern Recognition (CVPR)*, Jun. 2016, pp. 770–778, iISSN: 1063-6919.
- [14] S. Xie, R. Girshick, P. Dollár, Z. Tu, and K. He, “Aggregated Residual Transformations for Deep Neural Networks,” in *2017 IEEE Conference on Computer Vision and Pattern Recognition (CVPR)*. Honolulu, HI: IEEE, Jul. 2017, pp. 5987–5995, iISSN: 1063-6919.
- [15] M. Tan and Q. Le, “EfficientNet: Rethinking model scaling for convolutional neural networks,” in *Proceedings of the 36th International Conference on Machine Learning*, ser. Proceedings of Machine Learning Research, K. Chaudhuri and R. Salakhutdinov, Eds., vol. 97. PMLR, 09–15 Jun 2019, pp. 6105–6114.
- [16] —, “Efficientnetv2: Smaller models and faster training,” in *Proceedings of the 38th International Conference on Machine Learning*, ser. Proceedings of Machine Learning Research, M. Meila and T. Zhang, Eds., vol. 139. PMLR, 18–24 Jul 2021, pp. 10 096–10 106.
- [17] S. Woo, S. Debnath, R. Hu, X. Chen, Z. Liu, I. S. Kweon, and S. Xie, “ConvNeXt V2: Co-designing and Scaling ConvNets with Masked Autoencoders,” in *2023 IEEE/CVF Conference on Computer Vision and Pattern Recognition (CVPR)*. Vancouver, BC, Canada: IEEE, Jun. 2023, pp. 16 133–16 142, iISSN: 2575-7075.
- [18] Z. Liu, H. Mao, C.-Y. Wu, C. Feichtenhofer, T. Darrell, and S. Xie, “A ConvNet for the 2020s,” in *2022 IEEE/CVF Conference on Computer Vision and Pattern Recognition (CVPR)*. New Orleans, LA, USA: IEEE, Jun. 2022, pp. 11 966–11 976, iISSN: 2575-7075.
- [19] M. Oquab, T. Darcet, T. Moutakanni, H. Vo, M. Szafraniec, V. Khalidov, P. Fernandez, D. Haziza, F. Massa, A. El-Nouby, M. Assran, N. Ballas, W. Galuba, R. Howes, P.-Y. Huang, S.-W. Li, I. Misra, M. Rabbat, V. Sharma, G. Synnaeve, H. Xu, H. Jegou, J. Mairal, P. Labatut, A. Joulin, and P. Bojanowski, “DINOv2: Learning Robust Visual Features without Supervision,” Feb. 2024, arXiv:2304.07193 [cs].
- [20] F. Lu, X. Lan, L. Zhang, D. Jiang, Y. Wang, and C. Yuan, “CricaVPR: Cross-image Correlation-aware Representation Learning for Visual Place Recognition,” Apr. 2024, arXiv:2402.19231 [cs].
- [21] S. Izquierdo and J. Civera, “Optimal Transport Aggregation for Visual Place Recognition,” in *2024 IEEE/CVF Conference on Computer Vision and Pattern Recognition (CVPR)*, Jun. 2024, pp. 17 658–17 668, iISSN: 2575-7075.
- [22] F. Radenović, G. Tolias, and O. Chum, “Fine-tuning CNN Image Retrieval with No Human Annotation,” Jul. 2018, arXiv:1711.02512 [cs].
- [23] A. S. Razavian, J. Sullivan, S. Carlsson, and A. Maki, “Visual Instance Retrieval with Deep Convolutional Networks,” May 2016, arXiv:1412.6574 [cs].
- [24] G. Tolias, R. Sivic, and H. Jégou, “Particular object retrieval with integral max-pooling of CNN activations,” Feb. 2016, arXiv:1511.05879 [cs].
- [25] S. Lowry, N. Sünderhauf, P. Newman, J. J. Leonard, D. Cox, P. Corke, and M. J. Milford, “Visual Place Recognition: A Survey,” *IEEE Transactions on Robotics*, vol. 32, no. 1, pp. 1–19, Feb. 2016.
- [26] C. Masone and B. Caputo, “A Survey on Deep Visual Place Recognition,” *IEEE Access*, vol. 9, pp. 19 516–19 547, 2021.
- [27] G. Berton, R. Mereu, G. Trivigno, C. Masone, G. Csurka, T. Sattler, and B. Caputo, “Deep Visual Geo-localization Benchmark,” in *2022 IEEE/CVF Conference on Computer Vision and Pattern Recognition (CVPR)*. New Orleans, LA, USA: IEEE, Jun. 2022, pp. 5386–5397, iISSN: 2575-7075.
- [28] F. Schroff, D. Kalenichenko, and J. Philbin, “FaceNet: A unified embedding for face recognition and clustering,” in *2015 IEEE Conference on Computer Vision and Pattern Recognition (CVPR)*. Boston, MA, USA: IEEE, Jun. 2015, pp. 815–823, iISSN: 1063-6919.
- [29] X. Wang, X. Han, W. Huang, D. Dong, and M. R. Scott, “Multi-Similarity Loss With General Pair Weighting for Deep Metric Learning,” in *2019 IEEE/CVF Conference on Computer Vision and Pattern Recognition (CVPR)*. Long Beach, CA, USA: IEEE, Jun. 2019, pp. 5017–5025, iISSN: 2575-7075.
- [30] M. Leyva-Vallina, N. Strisciuglio, and N. Petkov, “Data-Efficient Large Scale Place Recognition with Graded Similarity Supervision,” in *2023 IEEE/CVF Conference on Computer Vision and Pattern Recognition (CVPR)*. Vancouver, BC, Canada: IEEE, Jun. 2023, pp. 23 487–23 496, iISSN: 2575-7075.
- [31] T. Weyand, I. Kostrikov, and J. Philbin, “PlaNet - Photo Geolocation with Convolutional Neural Networks,” in *Computer Vision – ECCV 2016*, B. Leibe, J. Matas, N. Sebe, and M. Welling, Eds. Cham: Springer International Publishing, 2016, pp. 37–55.
- [32] N. Vo, N. Jacobs, and J. Hays, “Revisiting IM2GPS in the Deep Learning Era,” in *2017 IEEE International Conference on Computer Vision (ICCV)*. Venice: IEEE, Oct. 2017, pp. 2640–2649, iISSN: 2380-7504.
- [33] G. Kordopatis-Zilos, P. Galopoulos, S. Papadopoulos, and I. Kompatsiaris, “Leveraging EfficientNet and Contrastive Learning for Accurate Global-scale Location Estimation,” in *Proceedings of the 2021 International Conference on Multimedia Retrieval*, ser. ICMR ’21. Taipei Taiwan: ACM, Aug. 2021, pp. 155–163.
- [34] J. Theiner, E. Muller-Budack, and R. Ewerth, “Interpretable Semantic Photo Geolocation,” in *2022 IEEE/CVF Winter Conference on Applications of Computer Vision (WACV)*. Waikoloa, HI, USA: IEEE, Jan. 2022, pp. 1474–1484, iISSN: 2642-9381.

- [35] M. Izbicki, E. E. Papalexakis, and V. J. Tsotras, "Exploiting the Earth's Spherical Geometry to Geolocate Images," in *Machine Learning and Knowledge Discovery in Databases*, U. Brefeld, E. Fromont, A. Hotho, A. Knobbe, M. Maathuis, and C. Robardet, Eds. Cham: Springer International Publishing, 2020, pp. 3–19.
- [36] E. Müller-Budack, K. Pustu-Iren, and R. Ewerth, "Geolocation Estimation of Photos Using a Hierarchical Model and Scene Classification," in *Computer Vision – Eccv 2018*, V. Ferrari, M. Hebert, C. Sminchisescu, and Y. Weiss, Eds. Cham: Springer International Publishing, 2018, pp. 575–592.
- [37] P. H. Seo, T. Weyand, J. Sim, and B. Han, "CPlaNet: Enhancing Image Geolocalization by Combinatorial Partitioning of Maps," in *Computer Vision – ECCV 2018*, V. Ferrari, M. Hebert, C. Sminchisescu, and Y. Weiss, Eds. Cham: Springer International Publishing, 2018, pp. 544–560.
- [38] P. Gronát, J. Sivic, G. Obozinski, and T. Pajdla, "Learning and Calibrating Per-Location Classifiers for Visual Place Recognition," *International Journal of Computer Vision*, vol. 118, no. 3, pp. 319–336, Jul. 2016.
- [39] G. Berton, C. Masone, and B. Caputo, "Rethinking Visual Geolocalization for Large-Scale Applications," in *2022 IEEE/CVF Conference on Computer Vision and Pattern Recognition (CVPR)*. New Orleans, LA, USA: IEEE, Jun. 2022, pp. 4868–4878.
- [40] H. Wang, Y. Wang, Z. Zhou, X. Ji, D. Gong, J. Zhou, Z. Li, and W. Liu, "CosFace: Large Margin Cosine Loss for Deep Face Recognition," Apr. 2018, arXiv:1801.09414 [cs].
- [41] G. Trivigno, G. Berton, J. Aragon, B. Caputo, and C. Masone, "Divide&Classify: Fine-Grained Classification for City-Wide Visual Place Recognition," Dec. 2023, arXiv:2307.08417 [cs].
- [42] S. Li, M. Hu, X. Xiao, and Z. Tu, "Patch similarity self-knowledge distillation for cross-view geo-localization," *IEEE Transactions on Circuits and Systems for Video Technology*, vol. 34, no. 6, pp. 5091–5103, 2024.
- [43] S. Li, Z. Tu, Y. Chen, and T. Yu, "Multi-scale attention encoder for street-to-aerial image geo-localization," *CAA Transactions on Intelligence Technology*, vol. 8, no. 1, p. 166–176, Jan. 2022.
- [44] C. Toft, W. Maddern, A. Torii, L. Hammarstrand, E. Stenborg, D. Safari, M. Okutomi, M. Pollefeys, J. Sivic, T. Pajdla, F. Kahl, and T. Sattler, "Long-Term Visual Localization Revisited," *IEEE Transactions on Pattern Analysis and Machine Intelligence*, vol. 44, no. 4, pp. 2074–2088, Apr. 2022.
- [45] S. Lynen, B. Zeisl, D. Aiger, M. Bosse, J. Hesch, M. Pollefeys, R. Siegwart, and T. Sattler, "Large-scale, real-time visual-inertial localization revisited," *International Journal of Robotics Research*, vol. 39, no. 9, pp. 1061–1084, Aug. 2020, publisher: SAGE Publications Ltd STM.
- [46] T. Naseer, W. Burgard, and C. Stachniss, "Robust Visual Localization Across Seasons," *IEEE Transactions on Robotics*, vol. 34, no. 2, pp. 289–302, Apr. 2018.
- [47] K. Amer, M. Samy, R. ElHakim, M. Shaker, and M. ElHelw, "Convolutional Neural Network-Based Deep Urban Signatures with Application to Drone Localization," in *2017 IEEE International Conference on Computer Vision Workshops (ICCVW)*, Oct. 2017, pp. 2138–2145, iSSN: 2473-9944.
- [48] K. Simonyan and A. Zisserman, "Very Deep Convolutional Networks for Large-Scale Image Recognition," Apr. 2015, arXiv:1409.1556 [cs].
- [49] B. Patel, T. D. Barfoot, and A. P. Schoellig, "Visual Localization with Google Earth Images for Robust Global Pose Estimation of UAVs," in *2020 IEEE International Conference on Robotics and Automation (ICRA)*, May 2020, pp. 6491–6497, iSSN: 2577-087X.
- [50] N. Samano, M. Zhou, and A. Calway, "Global Aerial Localisation Using Image and Map Embeddings," in *2021 IEEE International Conference on Robotics and Automation (ICRA)*, May 2021, pp. 5788–5794, iSSN: 2577-087X.
- [51] M. Mantelli, D. Pittol, R. Neuland, A. Ribacki, R. Maffei, V. Jorge, E. Prestes, and M. Kolberg, "A novel measurement model based on abBRIEF for global localization of a UAV over satellite images," *Robotics and Autonomous Systems*, vol. 112, pp. 304–319, Feb. 2019.
- [52] M. Bianchi and T. D. Barfoot, "UAV Localization Using Autoencoded Satellite Images," *IEEE Robotics and Automation Letters*, vol. 6, no. 2, pp. 1761–1768, Apr. 2021.
- [53] X. Meng, W. Guo, K. Zhou, T. Sun, L. Deng, S. Yu, and Y. Feng, "AirGeoNet: A Map-Guided Visual Geo-Localization Approach for Aerial Vehicles," *IEEE Transactions on Geoscience and Remote Sensing*, vol. 62, pp. 1–14, 2024.
- [54] C. Liu, S. Peng, S. Li, H. Qiu, Y. Xia, Z. Li, and L. Zhao, "A Novel EAGLe Framework for Robust UAV-View Geo-Localization," *IEEE Transactions on Geoscience and Remote Sensing*, vol. 63, pp. 1–17, 2025.
- [55] B. Sun, G. Liu, and Y. Yuan, "F3-Net: Multiview Scene Matching for Drone-Based Geo-Localization," *IEEE Transactions on Geoscience and Remote Sensing*, vol. 61, pp. 1–11, 2023.
- [56] M.-M. Gurgu, J. P. Queralta, and T. Westerlund, "Vision-Based GNSS-Free Localization for UAVs in the Wild," in *2022 7th International Conference on Mechanical Engineering and Robotics Research (ICMERR)*, Dec. 2022, pp. 7–12.
- [57] T. Lømo, J. Torresen, M. Kolberg, and R. Maffei, "Multi Map Visual Localization for Unmanned Aerial Vehicles," *IEEE Robotics and Automation Letters*, vol. 10, no. 2, pp. 1353–1360, Feb. 2025.
- [58] C. Chen, M. He, J. Wang, and Z. Meng, "Geocluster: Enhancing visual place recognition in spatial domain on aerial vehicle platforms," *IEEE Robotics and Automation Letters*, vol. 9, no. 3, pp. 3013–3020, March 2024.
- [59] S. Wang, R. She, Q. Kang, S. Li, D. Li, T. Geng, S. Yu, and W. P. Tay, "Multi-modal aerial-ground cross-view place recognition with neural odes," in *2025 IEEE/CVF Conference on Computer Vision and Pattern Recognition (CVPR)*, June 2025, pp. 11 717–11 728.
- [60] C. Li, M. He, C. Chen, J. Liu, X. Lyu, G. Huang, and Z. Meng, "GeoVins: Geographic-visual-inertial navigation system for large-scale drift-free aerial state estimation," *IEEE Transactions on Robotics*, vol. 41, pp. 5835–5853, 2025.
- [61] L. Yang, B. Kang, Z. Huang, Z. Zhao, X. Xu, J. Feng, and H. Zhao, "Depth Anything V2," Oct. 2024, arXiv:2406.09414.
- [62] L. Piccinelli, C. Sakaridis, Y.-H. Yang, M. Segu, S. Li, W. Abbeels, and L. V. Gool, "UniDepthV2: Universal Monocular Metric Depth Estimation Made Simpler," Feb. 2025, arXiv:2502.20110 [cs].
- [63] M. Hu, W. Yin, C. Zhang, Z. Cai, X. Long, H. Chen, K. Wang, G. Yu, C. Shen, and S. Shen, "Metric3D v2: A Versatile Monocular Geometric Foundation Model for Zero-Shot Metric Depth and Surface Normal Estimation," *IEEE Transactions on Pattern Analysis and Machine Intelligence*, vol. 46, no. 12, pp. 10 579–10 596, Dec. 2024.
- [64] S. F. Bhat, R. Birkel, D. Wofk, P. Wonka, and M. Müller, "ZoeDepth: Zero-shot Transfer by Combining Relative and Metric Depth," Feb. 2023, arXiv:2302.12288 [cs].
- [65] Z. Li, S. F. Bhat, and P. Wonka, "PatchFusion: An End-to-End Tile-Based Framework for High-Resolution Monocular Metric Depth Estimation," in *2024 IEEE/CVF Conference on Computer Vision and Pattern Recognition (CVPR)*. Seattle, WA, USA: IEEE, Jun. 2024, pp. 10 016–10 025, iSSN: 2575-7075.
- [66] A. Bochkovskii, A. Delaunoy, H. Germain, M. Santos, Y. Zhou, S. R. Richter, and V. Koltun, "Depth Pro: Sharp Monocular Metric Depth in Less Than a Second," Apr. 2025, arXiv:2410.02073 [cs].
- [67] H. Florea and S. Nedeveschi, "TanDepth: Leveraging Global DEMs for Metric Monocular Depth Estimation in UAVs," Sep. 2024, arXiv:2409.05142 [cs].
- [68] V.-C. Miclea and S. Nedeveschi, "Dynamic Semantically Guided Monocular Depth Estimation for UAV Environment Perception," *IEEE Transactions on Geoscience and Remote Sensing*, vol. 62, pp. 1–11, 2024.
- [69] M. Kim, A. K. Jain, and X. Liu, "AdaFace: Quality Adaptive Margin for Face Recognition," in *2022 IEEE/CVF Conference on Computer Vision and Pattern Recognition (CVPR)*. New Orleans, LA, USA: IEEE, Jun. 2022, pp. 18 729–18 738, version Number: 2.
- [70] J. Deng, J. Guo, J. Yang, N. Xue, I. Kotsia, and S. Zafeiriou, "ArcFace: Additive Angular Margin Loss for Deep Face Recognition," *IEEE Transactions on Pattern Analysis and Machine Intelligence*, vol. 44, no. 10, pp. 5962–5979, Oct. 2022, arXiv:1801.07698 [cs].